Theoretical Insights into the Ultrafast Deactivation Mechanism and Photostability of a Natural Sunscreen System

Omidyan, Reza; Shahrokh, Leila; Whittock, Abigail L.; Stavros, Vasilios G.

DOI:
10.1021/acs.jpca.3c02360

Document Version
Publisher's PDF, also known as Version of record

Citation for published version (Harvard):
Omidyan, R, Shahrokh, L, Whittock, AL & Stavros, VG 2023, 'Theoretical Insights into the Ultrafast Deactivation Mechanism and Photostability of a Natural Sunscreen System: Mycosporine Glycine', *The Journal of Physical Chemistry A*, vol. 127, no. 22, pp. 4880-4887. https://doi.org/10.1021/acs.jpca.3c02360

THE JOURNAL OF PHYSICAL CHEMISTRY A
A JOURNAL OF THE AMERICAN CHEMICAL SOCIETY

pubs.acs.org/JPCA

Article

Theoretical Insights into the Ultrafast Deactivation Mechanism and Photostability of a Natural Sunscreen System: Mycosporine Glycine

Reza Omidyan,* Leila Shahrokh, Abigail L. Whittock, and Vasilios G. Stavros*

Cite This: *J. Phys. Chem. A* 2023, 127, 4880−4887

Read Online

ACCESS | Metrics & More | Article Recommendations | Supporting Information

ABSTRACT: In this work, different levels of quantum computational models such as MP2, ADC(2), CASSCF/CASPT2, and DFT/TD-DFT have been employed to investigate the photophysics and photostability of a mycosporine system, mycosporine glycine (MyG). First of all, a molecular mechanics approach based on the Monte Carlo conformational search has been employed to investigate the possible geometry structures of MyG. Then, comprehensive studies on the electronic excited states and deactivation mechanism have been conducted on the most stable conformer. The first optically bright electronic transition responsible for the UV absorption of MyG has been assigned as the S_2 ($^1\pi\pi^*$) owing to the large oscillator strength (0.450). The first excited electronic state (S_1) has been assigned as an optically dark ($^1n\pi^*$) state. From the nonadiabatic dynamics simulation model, we propose that the initial population in the S_2 ($^1\pi\pi^*$) state transfers to the S_1 state in under 100 fs, through an S_2/S_1 conical intersection (CI). The barrierless S_1 potential energy curves then drive the excited system to the S_1/S_0 CI. This latter CI provides a significant route for ultrafast deactivation of the system to the ground state *via* internal conversion.

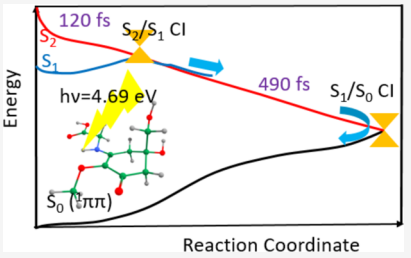

1. INTRODUCTION

Ultraviolet radiation (UVR) is the most energetic region of the broad spectrum of wavelengths from solar radiation that reaches the earth. This radiation is further subdivided into UVA (400−315 nm), UVB (315−280 nm), and UVC (280−100 nm).[1,2] Almost all the UVC and a large fraction of the UVB radiation are absorbed by the ozone layer in the stratosphere. This results in 5% UVB and 95% UVA accounting for the total UVR that reaches the earth's surface. These energy components have an impact on the earth's biosphere.[3] Although UVR can be beneficial, for example, the production of vitamin D being essential for prevention of skeletal disease,[4−6] there are lots of concerns regarding its hazardous effects on life.[7−10] The damaging effects of overexposure to UVR have been widely reported in previous studies and reviews, including cataract formation, skin aging, DNA mutation, and skin cancer.[11−15] Hence, the need for a balance between exposure to UVR and protection against overexposure to UVA and UVB is of crucial importance.[16]

There are different types of photoprotective compounds present on the market. Nevertheless, so far, no compound has proved to be exceptionally versatile. A major concern regarding photoprotective systems (sunscreens) is that some of the active ingredients within sunscreens are inherently not photostable. A well-known example of this issue is the UV filter avobenzone.[17] A good candidate for an efficient UV-filter (the active ingredient within sunscreens) should have efficient non-radiative decay and long-term photostability to dissipate the excess absorbed energy safely and quickly to regenerate the original ground-state molecule ready for reabsorption of another photon.[12]

Photoprotection in micro- and macroorganisms is achieved by a number of different molecules.[18] The particular family of molecules of interest here are mycosporines and mycosporine-like amino acids (MAAs). Mycosporines are derived from a cyclohexenone core, and MAAs are derived from a cyclohexenimine core.[19] Currently, there are over 70 mycosporines and MAAs isolated, and the various substituents on the ring, for example, the amino and imino functionalities, which are often amino acids or amino alcohols, are responsible for the wide range in peak absorption wavelength across both UVA and UVB regions of the electromagnetic spectrum.[20] These properties ideally lend themselves toward use in future cosmeceutical applications, largely due to the ability to tune the range (UVA and UVB) over which particular mycosporines and MAAs absorb. In contrast to the crucial photoprotection role that they have, rare reports in the literature are devoted to the fundamental root of the photophysical nature of these systems especially involving the cyclohexenone core.[21−23] Recent studies on MAAs clearly show that the excited electronic states are very short-lived, decaying rapidly to repopulate the ground electronic state. However understanding of the mechanisms of the relaxation dynamics in mycosporines and MAAs is still in its infancy.[24,25]

Received: April 8, 2023
Revised: May 5, 2023
Published: May 30, 2023

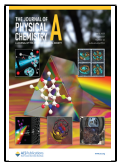

Herein, we report on a systematic investigation of the photochemical mechanisms for radiationless excited-state deactivation of the most stable conformer of mycosporine-glycine (abbreviated as MyG henceforth). This system has an absorption maximum at 310 nm in water solvent medium[26] and possesses a cyclohexenone ring linked with an amino acid, glycine (Figure 1). However, to the best of our knowledge, there are no reports on the spectroscopy of this system in the gas phase. The motivation behind such studies is that it allows us to distinguish between intrinsic molecular properties and properties resulting from the biological environment.[23,27] The details of fundamental biochemical characteristics and interactions are often hidden by macroscopic solvent effects and interactions with other molecules. Thus, studying individual biomolecules in vacuum reveals the intrinsic properties of the most basic biomolecular processes.[27,28]

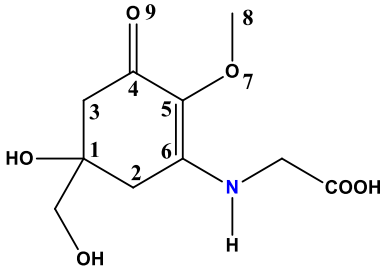

Figure 1. Chemical structure and numbering pattern of MyG applied in this work. Hydrogen atoms over the ring and other C atoms have been omitted for clarity.

In the present study, we explored the relevant excited-state potential-energy functions along a photochemical reaction path and optimized the relevant conical intersections (CIs) involved in the deactivation process. We have performed these explorations with the ADC(2) and CASSCF electronic-structure methods. In addition to the static exploration of the excited-state potential-energy profiles, we report the results of nonadiabatic trajectory-surface-hopping molecular dynamics simulations of MyG. Taking the implicit ethanol solvent model into account, the dynamics simulations were performed with the TD-DFT electronic-structure method, which is the method of choice for systems of this size.

2. COMPUTATIONAL DETAILS

The conformational landscapes of MyG have been determined based on the Monte Carlo multiple minimum (MCMM) methodology[29] using the MacroModel suite of program (version 8.5).[29] This initial exploration of the PES was done using classical molecular mechanics force fields (MMFFs).[30] The optimized geometry of selected conformers of the ground state and corresponding vibrational frequencies have been determined either at the density functional theory (DFT)/B3LYP or RI-MP2 level of theory using the cc-pVDZ basis set.[31] The vertical and adiabatic excitation energies of the lowest excited singlet states and oscillator strengths for electronic transitions were computed based on the RI-ADC(2), TD-DFT/ωB97XD,[32] and multistate complete active space second-order perturbation (MS-CASPT2)[33] theory. The RI-MP2 and RI-ADC(2) calculations were carried out by the Turbomole program suit (V 6.3.1).[34,35] The DFT and TD-DFT calculations were employed using the Gaussian 16 program,[36] and CASSCF/CASPT2[37,38] computations were performed using OpenMolcas (V 18.09).[39,40]

We have determined the potential energy curves representing the deactivation mechanism of our selected system based on linear interpolation in internal coordinates (LIIC). Our method of choice in this case is ADC(2) because of its reliability from our previous works along with works from other groups.[41−46] In addition, CI geometries were optimized using a state-averaged complete active space self-consistent field (SA-CASSCF).[47]

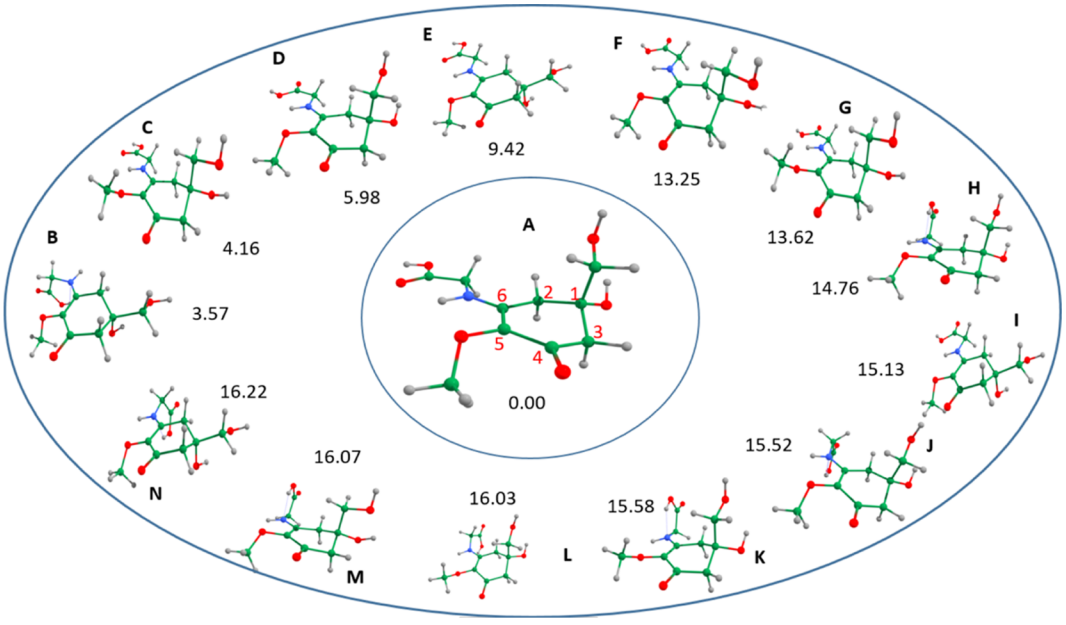

Figure 2. Optimized structures of the 14 most stable structures of MyG at the B3LYP/cc-pVDZ level of theory (the energetic values have been corrected by ZPE). The most stable structure (MyG-A) is shown in the center with other structures labeled according to decreasing stability. Their energies (in kJ mol^{-1}) are relative to MyG-A.

https://doi.org/10.1021/acs.jpca.3c02360
J. Phys. Chem. A 2023, 127, 4880−4887

Table 1. Vertical Transition Energies and Oscillator Strengths for the Most Stable Conformer MyG-A in the Gas Phase, Determined at the TD-ωB97XD, ADC(2), and MS-CASPT2 Levels of Theory with cc-pVDZ Basis Sets[a]

transition energy/eV (MyG-A)	TD-ωB97XD		ADC(2)		MS-CASPT2	
excited state	ΔE (f)	character	ΔE (f)	character	ΔE (f)	character
S_1	4.157 (0.0059)	$n\pi_1^*$	4.031 (0.0004) **2.86**[b]	$n\pi_1^*$	4.050 (0.000)	$n\pi_1^*$
S_2	4.709 (0.3922)	$\pi\pi_1^*$	4.693 (0.4497)	$\pi\pi_1^*$	4.680 (0.7600)	$\pi\pi_1^*$
S_3	5.512 (0.0131)	$\pi\pi_2^*$	6.182 (0.0066)	$\pi\pi_2^*$	7.150 (0.011)	$\pi\pi_2^*$
S_4	6.097 (0.0005)	$n\pi_2^*$	6.264 (0.0005)	$n\pi_2^*$	7.540 (0.003)	$n\pi_2^* + n\sigma^*$

[a]The MS-CASPT2 results have been obtained based on 8 electrons and 8 orbitals as the active space and 5 multistates. [b]Adiabatic $S_1 \leftarrow S_0$ transition energy determined at the optimized S_1 geometry of MyG-A. Further information regarding the MOs and transition characters could be found in Table S3, Supporting Information file.

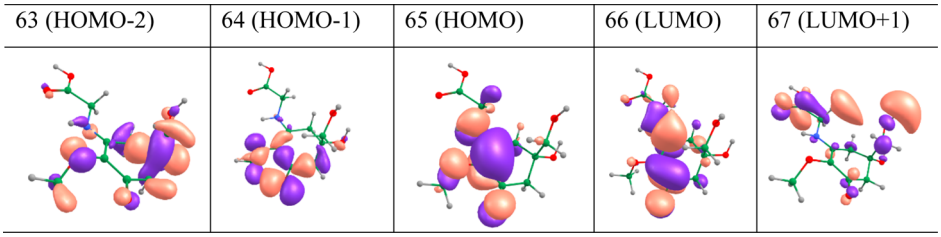

Figure 3. Selected valance MOs of MyG-A, determined at the SCF/cc-pVDZ level of theory, playing a prominent role in the lowest lying electronic transitions.

Moreover, determination of the UV absorption spectrum and nonadiabatic dynamics simulation have been conducted based on the TD-DFT model using Newton-X (V. 2.0)[48] interfaced with Gaussian 16. The validity of the selected model for determining the excited-state deactivation processes has been confirmed in different reports.[16,49−52] To perform nonadiabatic dynamics simulations, the initial conditions were computed for geometry and nuclear momenta sampled from a Wigner distribution based on the S_0 normal modes. Vertical excitation energies were computed at the ωB97XD/6-31G* level, and these energies were obtained with $\delta = 0.05$ eV Lorentzian line broadening for the two lowest singlet excited states.

In addition, to investigate the solvent's influence on absorption spectra, the polarizable continuum model (PCM/ethanol model)[53] implemented in Gaussian 16 has been used.

3. RESULTS AND DISCUSSION

3.1. Ground-State Optimized Geometries. The conformational flexibility of MyG mainly arises from (1) the −glycine side chain, (2) the −methoxy group ($-OCH_3$), (3) the hydroxymethyl group ($-CH_2OH$), and (4) flexible carbon sites of the ring. The orientation in space of the glycine side chain with respect to the six-membered ring could be subject to diversity in conformation in addition to location of its own atoms with respect to each other. Over the cyclohexenone ring, there are two double bonds, $C_5{=}C_6$ and $C_4{=}O_9$; thus, the C_4, C_5, and C_6 locates mainly in the same plane owing to the sp^2 hybridization nature of the C atoms (see Figure 1 for numbering). Other carbon atoms in the ring (C_1, C_2, and C_3) are sp^3-hybridized, and there are two possibilities for out-of-plane location of the C_1 atom and its subgroups; it could be pointing upward or pointing downward of the ring. Consequently, this offers another root of obtaining new conformations.

The conformational landscape of MyG has been determined based on the conformation search algorithm using the MCMM methodology. MMFFs were used for 1000 steps. All structures generated with energies within 20.0 kJ mol^{-1} of the minimum were examined. Based on the MCMM theoretical model, 101 conformers have been obtained. We have selected 30 of the most stable structures and determined the minimum geometry and consequently the relative stabilities based on the DFT method (at the B3LYP/cc-pVDZ level). Optimized geometries of the selected lowest-lying conformers (in energy) are presented in Figure 2. As shown, we have called the most stable structure MyG-A, which is 3.57 kJ mol^{-1} more stable than the next nearest conformer (at the B3LYP/cc-pVDZ level of theory, taking the ZPE correction into account). Comprehensive information regarding the 30 conformers is also presented in Table S1, Supporting Information file.

As shown in Figure 2, MyG-A exhibits a puckering feature around C_1. The dihedral angle of $C_1{-}C_2{-}C_3{-}C_4$ describing this deformation from the ring has been predicted at 49°. Other carbon sites of the six-membered ring stay roughly on the same plane; thus, the system looks like a half-chair. In addition, the dihedral angle of $C_{15}{-}O_{10}{-}C_5{-}C_6$ describing the position of the $-O-CH_3$ side chain with respect to the cyclohexenone ring has been predicted at 115° which is near-perpendicular (downward). The glycine side chain remains in the same plane with respect to the six-membered cyclohexenone ring. Moreover, from inspection of Figure 2, it is apparent that the out-of-plane deformation of C_1 above the molecular plane is present in several structures (for instance, A, C, D *etc.*), while its out-of-plane deformation below the molecular plane is also significantly populated (such as B, E, I, L, and N). Furthermore, when the glycine side chain remains in the molecular plane, the corresponding conformers are significantly more stable than those that have other orientations (such as K, L, M, and N).

To note, we have optimized the 6 most stable conformers based on the MP2/cc-pVDZ theoretical model, with their relative stabilities confirming the DFT level results. The optimized structure of the most stable MyG-A conformer at the MP2 level has been determined to be fairly similar to that found with DFT, with slight differences in the angles and

https://doi.org/10.1021/acs.jpca.3c02360
J. Phys. Chem. A 2023, 127, 4880−4887

Table 2. Vertical transition energies and oscillator strengths for lowest lying electronic transitions in the five most stable conformers of MyG[a]

	transition energy/eV (TD-ωB97XD/cc-pVDZ)				
excited state	MyG-A	MyG-B	MyG-C	MyG-D	MyG-E
			Gas Phase		
S_1 ($n\pi_1^*$)	4.157 (0.0059)	4.091 (0.0062)	4.083 (0.0051)	4.018 (0.0057)	4.165 (0.0098)
S_2 ($\pi\pi_1^*$)	4.709 (0.3922)	4.709 (0.391)	4.749 (0.3956)	4.593 (0.3828)	4.7421 (0.3974)
S_3 ($\pi\pi_2^*$)	5.512 (0.0131)	5.460 (0.0125)	5.525 (0.0102)	5.453 (0.0129)	5.419 (0.0161)
S_4 ($n\pi_2^*$)	6.097 (0.0005)	6.091 (0.0005)	6.095 (0.0005)	5.692 (0.0016)	6.0921 (0.0005)
			PCM/Ethanol		
S_1 ($n\pi_1^*$)	4.336 (0.0327)	4.279 (0.0298)	4.266 (0.0245)	4.206 (0.0320)	4.328 (0.0414)
S_2 ($\pi\pi_1^*$)	4.603 (0.4513)	4.594 (0.4543)	4.630 (0.4613)	4.485 (0.4403)	4.662 (0.4608)
S_3 ($\pi\pi_2^*$)	5.898 (0.0112)	5.873 (0.0103)	5.921 (0.0090)	5.704 (0.0066)	5.867 (0.0110)
S_4 ($n\pi_2^*$)	6.191 (0.0006)	6.189 (0.0006)	6.193 (0.0006)	5.862 (0.0007)	6.443 (0.0397)

[a]Calculations were performed in the gas phase and in the PCM/ethanol implicit solvent, determined at the TD-ωB97XD/cc-pVDZ level of theory.

dihedrals, especially in the glycine side chain. Comparison of the optimized MP2 and DFT/B3LYP structure of MyG-A is shown in Figure S1 of the Supporting Information.

From our conformational study, we have selected the most stable conformer (MyG-A) and concentrated on its electronic structure, excited states, and deactivation mechanism which now follows.

3.2. Electronic Transition Energies. Calculated vertical transition energies and oscillator strengths of the most stable conformer, MyG-A, to the four lowest lying singlet excited states (S_1−S_4) have been determined and are presented in Table 1. We have employed different levels of theory: TD-DFT using the ωB97XD functional; RI-ADC(2); and MS-CASPT2. Regarding the TD-DFT calculations, the ωB97XD functional was used as it successfully described the energy of the electronic states and nonradiative deactivation process in similar systems.[24,49,51,54−56]

Selected valence molecular orbitals (MOs) of MyG-A are presented in Figure 3. According to our ADC(2) results, the $S_1 \leftarrow S_0$ electronic transition has been assigned as an optically dark ($^1n\pi^*$) transition, originating from LUMO ← HOMO − 1 (85%) single-electron transitions. The HOMO and LUMO, respectively, stand for the highest occupied molecular orbital and the lowest unoccupied molecular orbital. The second singlet electronic transition (the $S_2 \leftarrow S_0$) has been assigned as an optically bright $^1\pi\pi^*$ transition, involving a LUMO ← HOMO transition (92%). As the molecular point group is C1 (and there is no symmetry plane), our assignments are only qualitative.

The MOs involving the $S_3 \leftarrow S_0$ electronic transition have been assigned mainly as LUMO + 1 ← HOMO and LUMO + 2 ← HOMO transitions, and for $S_4 \leftarrow S_0$, the LUMO ← HOMO − 3 transition has been predicted to be the main contributor. More information regarding the electronic transitions and contributing MOs can be found in the Supporting Information.

The MS-CASPT2 results have been obtained, selecting the 8 electrons and 8 valance orbitals (4 occupied and 4 virtual) as the active space (see Table S2, Supporting Information). We have examined different active spaces to determine the vertical transition energies. As the S_2−S_0, $^1\pi\pi^*$ electronic transition dominates the photophysics of MyG, we have selected the active space yielding the most reliable result for this electronic transition. Although there is no experimental UV absorption spectrum of MyG in the gas phase, as mentioned before, the λ_{max} of absorption around 300 nm has been reported for MyG in water solution. The active space of (8, 8) gives better results than others, and no improvement has occurred considering the larger active spaces (see Table S4, Supporting Information file).

As shown in Table 1, the MS-CASPT2 results for S_1 and S_2 states are comparable with the ADC(2) and also TD-DFT/ωB97XD results. There is a discrepancy relating to the $S_3 \leftarrow S_0$ electronic transition energy which is significantly underestimated at the TD-DFT level. However, due to the optically dark nature of this state (low oscillator strength), it should have no significant bearing on the photophysics of MyG. The energetic value of the $S_2 \leftarrow S_0$ transition ($^1\pi\pi^*$), responsible for the UV absorption of MyG-A, has been determined as 4.71, 4.69, and 4.68 eV, respectively, at the TD-ωB97XD, RI-ADC(2), and MS-CASPT2 levels of theory. Good agreement of TD-ωB97XD results with RI-ADC(2) and MS-CASPT2 (especially for the S_1 and S_2 transition energies) indicates that this functional is sufficiently reliable to describe electronic structures of the selected systems.

To perform a comparison between the five most stable structures of MyG-(A, B, C, D, and E), we have determined the vertical electronic transition energies in the gas phase and also with the implicit ethanol solvent for the four lowest lying singlet excited states at the TD-ωB97XD/cc-pVDZ level of theory. The results are presented in Table 2. Inspection of these results reflects at least two important points:

(1) The electronic transition energies of the five most stable conformers of MyG are quite close to each other. This indicates that the photophysics of these systems should be similar.

(2) The electronic transition energies in the implicit solvent (ethanol) are mildly different from the corresponding gas-phase results. Consistent with previous results,[57] it indicates that the solvent effect on the photophysical nature of these systems would be negligible.

To garner more insights into the exited-state nature of MyG-A, we have performed the RI-ADC(2) geometry optimizations for the excited S_1 and S_2 states. As mentioned *supra*, the S_1 is an optically dark state having $^1n\pi^*$ character and roughly zero oscillator strength. The S_2 ($^1\pi\pi^*$) state is responsible for the UV absorption of MyG (F = 0.450 in MyG-A). The S_1 excited state exhibits a local minimum, with a molecular geometry that is significantly different from that of the ground state (see Figure 4a,b). The glycine side chain exhibits an out-of-plane movement, and there is a slight distortion of the ring around

https://doi.org/10.1021/acs.jpca.3c02360
J. Phys. Chem. A 2023, 127, 4880−4887

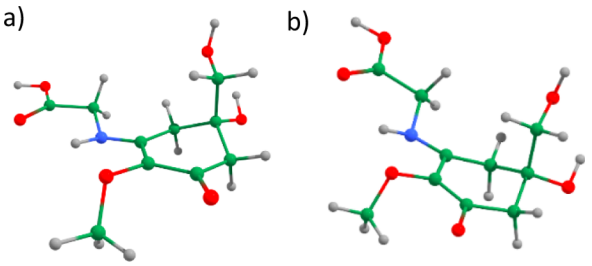

Figure 4. Optimized geometries of (a) S_0 ground state and (b) S_1 ($^1n\pi^*$) state determined, respectively, at the MP2 and ADC(2) theoretical levels.

the C_6 and C_3 regions. These changes in geometry stabilize the S_1 excited state, so that the adiabatic $S_1 \leftarrow S_0$ transition energy has been predicted to be significantly lower (2.86 eV) than its vertical analogue (4.03 eV). Furthermore, our calculations predict no local minimum on the S_2 potential energy surface, and the S_2 geometry optimization results in strong deformation of the six-membered ring from the C_6 carbon site and other side chains.

3.3. Photophysical Behaviors: CIs and Potential Energy Profiles. To gain more insights into the excited-state relaxation mechanism of MyG-A, we have searched for possible CIs. We have located two CIs for MyG-A based on the SA-CASSCF(6,6)/cc-pVDZ theoretical model (see Figure 5a,b). The active space in the SA-CASSCF calculations contains 6 electrons in 6 MOs (3 occupied and 3 virtual MOs, Table S2, Supporting Information). The CI_1 represents the S_2/S_1 potential energy crossing, and the CI_2 describes the minimum structure of the S_1/S_0 curve crossing. As shown in Figure 5, both optimized CI structures exhibit puckering of the ring at C_6, in addition to out-of-plane movement of the glycine moiety. This deformation is more pronounced in CI_2. Moreover, there is a significant alteration in the $C_8-O_7-C_5-C_6$ dihedral angle (from 115.6° in the ground state to −113.7°). On the other hand, in CI_2, the methoxy ($-OCH_3$) group moves toward the glycine side chain (upward the ring). This alteration is accompanied by a slight out-of-plane distortion of C_5 downward the ring. The optimized Cartesian coordinates of the CIs are presented in the Supporting Information.

It is well known that locating CIs does not warrant the nonradiative deactivation process since the presence of a large barrier could prevent this deactivation pathway. Thus, we have determined potential energy (PE) profiles for the ground and two electronic excited states (S_1 and S_2) based on the LIIC connecting the Franck−Condon (FC) region of MyG-A to CI_2. The results are presented in Figure 5. As shown, the S_1 and S_2 potential energy profiles decrease in energy along the LIIC coordinate. The S_2 potential energy curve first crosses with the S_1 potential energy curve (obtaining the CI_1 in the multidimensional picture).

This trend continues until the end of the reaction coordinate. The ground-state PE profile increases in energy along the LIIC coordinate, ultimately crossing the S_1 PE profile. As shown, the S_1 PE curve starting from the FC region passes through a shallow local minimum and then increases to cross with the S_2 PE curve. This local minimum in the LIIC potential energy profile is in accordance with the results of obtaining a minimum geometry for the S_1 state as discussed *supra*. The S_1/S_0 curve crossing at the end of the reaction coordinate provides an essential root for ultrafast deactivation of the excited state based on internal conversion to the ground-state S_0 potential energy surface. Since the predicted CI (around 3.0 eV) is located significantly lower than the S_2 vertical transition energy [of 4.69 eV at the ADC(2) level], one could envisage that excited-state population in S_2 will approach the CI especially since the S_2 PE profile is purely repulsive.

One may be concerned that ADC(2), as a single-reference method, would not be reliable enough to describe the photophysical nature, especially the S_1/S_0 CI of MyG-A. To address this concern, we have determined the ground- and excited-state potential energy profiles of MyG-A along the

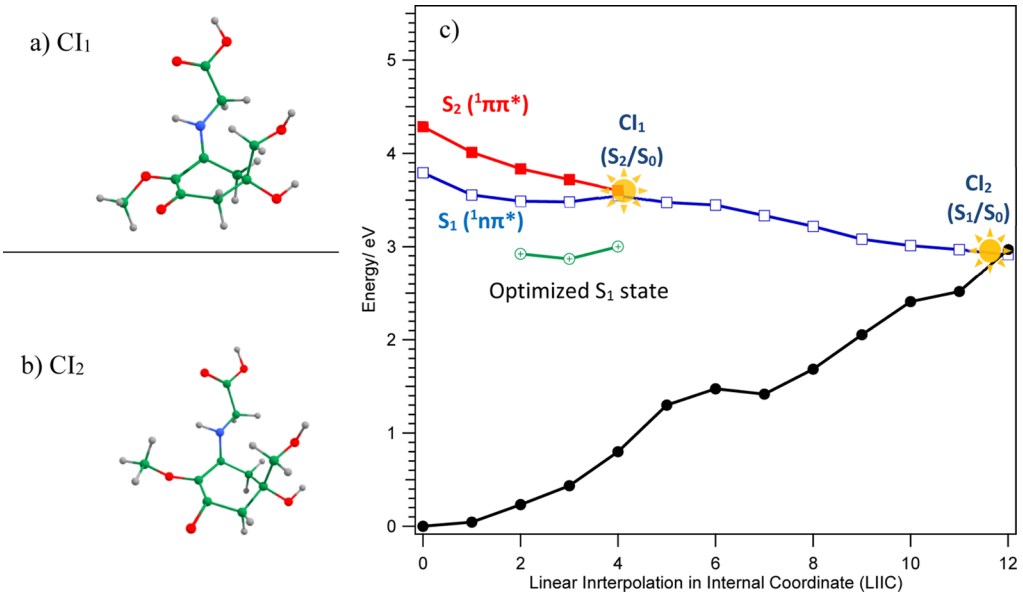

Figure 5. Optimized geometries of the CIs located for MyG-A: (a) CI_1 (S_2/S_1) and (b) CI_2 (S_1/S_0) determined at the SA-CASSCF(6,6)/cc-pVDZ theoretical level. (c) PE profile of the ground (black) and 2 singlet excited states of MyG-A calculated at the ADC(2)/cc-pVDZ level of theory along the LIIC reaction path.

https://doi.org/10.1021/acs.jpca.3c02360
J. Phys. Chem. A 2023, 127, 4880−4887

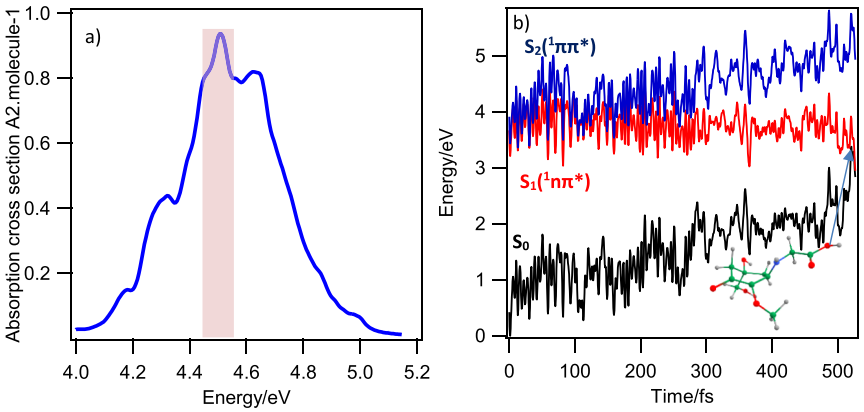

Figure 6. (a) UV absorption spectrum simulated at the TD-ωB97XD/6-31G* method based on the $S_2 \leftarrow S_0$ electronic transition in the PCM/ethanol implicit solvent with 300 points for MyG-A. (b) Energy profiles of a selected trajectory for MyG-A. The black, red, and blue curves, respectively, indicate the ground (S_0), S_1, and S_2 excited states. The inset in panel a represents the geometry of S_1/S_0 CI (out-of-plane movement of glycine as the prominent alteration).

LIIC coordinate (corresponding to Figure 5), based on the MS-CASPT2/CASSCF(6,6)/cc-pVDZ theoretical model. The results have been presented in Figure S2, Supporting Information file. As shown, the CASPT2 results support the validity of our ADC(2) theoretical results. To add, previous reports have also demonstrated that ADC(2) results are qualitatively reliable in describing the photophysics of organic systems.[41,42,44,46,58−60]

3.4. Nonadiabatic Dynamics Simulations Results. In order to shed more light into the relaxation dynamics of MyG, we have employed the nonadiabatic dynamics simulation based on the TD-DFT theoretical model on the most stable conformer, MyG-A. In this regard, a nonadiabatic surface hopping dynamics simulation was performed from the second excited-state S_2 ($^1\pi\pi^*$) at the TD-ωB97xD/6-31G* level of theory, with ethanol as the implicit solvent.

The photoabsorption spectrum of MyG-A, shown in Figure 6, was simulated using the nuclear ensemble approach.[61] The velocity Verlet[62] algorithm with a time step of 0.5 fs was used for the integration of Newton's equations. Since the first bright state in MyG-A is the S_2 ($^1\pi\pi^*$) state, the nonadiabatic dynamics simulation has been started from S_2, using the decoherence-corrected[63] fewest switches surface hopping (DC-FSSH) approach.[64] A total of 52 trajectories starting from the optically bright S_2 state were considered. The initial conditions for the dynamics were sampled within the 4.55 ± 0.10 eV spectral window highlighted in Figure 6. We considered that a trajectory went back to the ground-state S_0 when the S_1-S_0 energetic gap approached a threshold of 0.25 eV.

Surface hopping dynamics was simulated for a maximum of 1000 fs with a nuclear time step of 0.50 fs. 100% of optically bright S_2 ($^1\pi\pi^*$)-state population is transferred to the S_1 ($^1n\pi^*$) state within the initial ∼120 fs of the dynamics. Therefore, the deactivation mechanism starts at the S_2 ($^1\pi\pi^*$) state, with excited-state population traversing the S_2/S_1 CI in around 120 fs, leading the excited system to drive over the S_1 PE curve ending by CI_2 (see Figure 6b). This later CI provides an essential root for ultrafast internal conversion of the excited system to the ground state. Consequently, the net effect of this process would be converting the hazardous UV light (of 4.69 eV) to harmless vibrational motion (or heat). The dynamics results are in good agreement with our previously discussed *ab initio* results.

From the results of the dynamics, we predict that 82% of the trajectories relax based on the ring puckering from the C_6 region (corresponding to CI_2 presented in Figure 5b) as well as the C_3 region. Moreover, 10% trajectories have been assigned to relax with ring puckering from C_1 and C_4 carbon sites.

To conclude this section, we present the time evolution of the nonadiabatic population of the ground and the first two excited states from the nonadiabatic dynamics simulation of MyG-A (Figures S3 and S4, Supporting Information). Using a sigmoid curve fitting procedure[56] as an approximate guide, we determine that the S_2 excited-state lifetime; τ_{S_2} is predicted to be ∼67 fs, while the S_1 excited-state lifetime, τ_{S_1}, is predicted to be ∼517 fs. Further details regarding this fitting is presented in Supporting Information, Figure S2. From this, we conclude that photoexcitation of MyG to S_2 can relax to the S_0 ground state in approximately $\tau_{S_2} + \tau_{S_1}$ = 584 fs. This ultra-short lifetime of the excited state is in accordance with the high photostability of MyG-A.

4. SUMMARY AND CONCLUSIONS

Molecular mechanics configurational search has been employed to determine the possible structures and conformers of mycosporine glycine. We have employed stepwise computational models to determine the lowest lying conformers and consequently the most stable structure. Following this, state-of-the-art *ab initio* computational models as well as nonadiabatic dynamics simulations have been conducted to shed light on the photophysics of MyG. We show that the S_2 ($^1\pi\pi^*$) state is responsible for the UV absorption. Following photoabsorption in the UV region [4.69 eV at the ADC(2) theoretical level], excited population proceeds along a ring twisting reaction coordinate, traversing through the S_2/S_1 CI. This takes place on the order of 100 fs. We have also shown that the potential energy profile of the S_1 state after the S_2/S_1 CI significantly decreases in energy and thus drives the excited system to the S_1/S_0 CI. This CI governs the ultrafast deactivation of the excited system to the ground state by internal conversion. These results provide significant molecular level insights into the origins of photostability of MyG and consequently its ability to photoprotect microorganisms against the potentially detrimental effects of UV radiation exposure. These results also provide benchmark data that could be used to develop next-generation UV filters for commercial applications.

https://doi.org/10.1021/acs.jpca.3c02360
J. Phys. Chem. A 2023, 127, 4880−4887

■ ASSOCIATED CONTENT

Supporting Information

The Supporting Information is available free of charge at https://pubs.acs.org/doi/10.1021/acs.jpca.3c02360.

Optimized geometry (along with relative energy in kJ mol^{-1}) for 30 selected conformers of MyG, valance MOs contributing to the SA-CASSCF calculations of this work, *xyz* coordinates, lowest-lying transition energies, relevant MOs, and additional information about potential energy surfaces and time evolution of the nonadiabatic population of the ground state and first excited state from nonadiabatic dynamics simulation for MyG-A (PDF)

■ AUTHOR INFORMATION

Corresponding Authors

Reza Omidyan − *Department of Chemistry, University of Isfahan, Isfahan 81746-73441, Iran*; Email: r.omidyan@sci.ui.ac.ir

Vasilios G. Stavros − *Department of Chemistry, University of Warwick, Coventry CV4 7AL, U.K.; School of Chemistry, University of Birmingham, Birmingham B15 2TT, U.K.*; orcid.org/0000-0002-6828-958X; Email: v.stavros@warwick.ac.uk

Authors

Leila Shahrokh − *Department of Chemistry, University of Isfahan, Isfahan 81746-73441, Iran*

Abigail L. Whittock − *Department of Chemistry and Analytical Science Centre for Doctoral Training, Senate House, University of Warwick, Coventry CV4 7AL, U.K.*; orcid.org/0000-0001-6361-3291

Complete contact information is available at: https://pubs.acs.org/10.1021/acs.jpca.3c02360

Notes

The authors declare no competing financial interest.

■ ACKNOWLEDGMENTS

The research council of the University of Isfahan is kindly appreciated for financial support. The use of the computing facility cluster GMPCS of the LUMAT federation (FR LUMAT2764) is acknowledged. A.L.W. thanks the University of Warwick and Lubrizol for funding through the Centre for Doctoral Training in Analytical Science. V.G.S. thanks the Royal Society for a Royal Society Industry Fellowship.

■ REFERENCES

(1) Lacis, A. A.; Hansen, J. A parameterization for the absorption of solar radiation in the earth's atmosphere. *J. Atmos. Sci.* **1974**, *31*, 118−133.

(2) Frederick, J. E.; Snell, H. E.; Haywood, E. K. Solar ultraviolet radiation at the earth's surface. *Photochem. Photobiol.* **1989**, *50*, 443−450.

(3) Matsumi, Y.; Kawasaki, M. Photolysis of atmospheric ozone in the ultraviolet region. *Chem. Rev.* **2003**, *103*, 4767−4782.

(4) Holick, M. F. Sunlight And Vitamin D for Bone Health and Prevention of Autoimmune Diseases, Cancers, and Cardiovascular Disease. *Am. J. Clin. Nutr.* **2004**, *80*, S1678−S1688.

(5) Mithal, A.; Wahl, D. A.; Bonjour, J. P.; Burckhardt, P.; Dawson-Hughes, B.; Eisman, J. A.; El-Hajj Fuleihan, G.; Josse, R. G.; Lips, P.; Morales-Torres, J. Global vitamin D status and determinants of hypovitaminosis D. *Osteoporosis Int.* **2009**, *20*, 1821.

(6) Lips, P.; van Schoor, N. M. The effect of vitamin D on bone and osteoporosis. *Best Pract. Res., Clin. Endocrinol. Metab.* **2011**, *25*, 585−591.

(7) Humble, M. B. Vitamin D, light and mental health. *J. Photochem. Photobiol., B* **2010**, *101*, 142−149.

(8) Wlaschek, M.; Tantcheva-Poór, I.; Naderi, L.; Ma, W.; Schneider, L. A.; Razi-Wolf, Z.; Schüller, J.; Scharffetter-Kochanek, K. Solar UV irradiation and dermal photoaging. *J. Photochem. Photobiol., B* **2001**, *63*, 41−51.

(9) Battie, C.; Jitsukawa, S.; Bernerd, F.; Del Bino, S.; Marionnet, C.; Verschoore, M. New insights in photoaging, UVA induced damage and skin types. *Exp. Dermatol.* **2014**, *23*, 7−12.

(10) Encinas Perea, S. Solar Filters: A Strategy of Photoprotection. In *Applied Photochemistry: When Light Meets Molecules*; Bergamini, G., Silvi, S., Eds.; Springer International Publishing: Cham, 2016; pp 459−478.

(11) Baker, L. A.; Marchetti, B.; Karsili, T. N. V.; Stavros, V. G.; Ashfold, M. N. R. Photoprotection: extending lessons learned from studying natural sunscreens to the design of artificial sunscreen constituents. *Chem. Soc. Rev.* **2017**, *46*, 3770−3791.

(12) Rodrigues, N. d. N.; Woolley, J. M.; Krokidi, K. M.; Tesa-Serrate, M. A.; Turner, M. A. P.; Hine, N. D. M.; Stavros, V. G. Effects of substituent position on aminobenzoate relaxation pathways in solution. *Phys. Chem. Chem. Phys.* **2021**, *23*, 23242−23255.

(13) Gallagher, R. P.; Lee, T. K. Adverse effects of ultraviolet radiation: A brief review. *Prog. Biophys. Mol. Biol.* **2006**, *92*, 119−131.

(14) Taylor, H. R.; West, S. K.; Rosenthal, F. S.; Muñoz, B.; Newland, H. S.; Abbey, H.; Emmett, E. A. Effect of ultraviolet radiation on cataract formation. *N. Engl. J. Med.* **1988**, *319*, 1429−1433.

(15) Narayanan, D. L.; Saladi, R. N.; Fox, J. L. Review: Ultraviolet radiation and skin cancer. *Int. J. Dermatol.* **2010**, *49*, 978−986.

(16) Shick, J. M.; Dunlap, W. C. Mycosporine-like amino acids and related Gadusols: biosynthesis, acumulation, and UV-protective functions in aquatic organisms. *Annu. Rev. Physiol.* **2002**, *64*, 223−262.

(17) Mturi, G. J.; Martincigh, B. S. Photostability of the sunscreening agent 4-tert-butyl-4′-methoxydibenzoylmethane (avobenzone) in solvents of different polarity and proticity. *J. Photochem. Photobiol., A* **2008**, *200*, 410−420.

(18) Saewan, N.; Jimtaisong, A. Natural products as photoprotection. *J. Cosmet. Dermatol.* **2015**, *14*, 47−63.

(19) M. Bandaranayake, W. Mycosporines: are they nature's sunscreens? *Nat. Prod. Rep.* **1998**, *15*, 159−172.

(20) Geraldes, V.; Pinto, E. Mycosporine-like amino acids (maas): biology, chemistry and identification features. *Pharmaceutical* **2021**, *14*, 63.

(21) Losantos, R.; Funes-Ardoiz, I.; Aguilera, J.; Herrera-Ceballos, E.; García-Iriepa, C.; Campos, P. J.; Sampedro, D. Rational Design and Synthesis of Efficient Sunscreens To Boost the Solar Protection Factor. *Angew. Chem., Int. Ed.* **2017**, *56*, 2632−2635.

(22) Losantos, R.; Churio, M. S.; Sampedro, D. Computational exploration of the photoprotective potential of gadusol. *Chem. Open* **2015**, *4*, 155−160.

(23) Hatakeyama, M.; Nakamura, S. Intrinsic nature of the ultrafast deexcitation pathway of Mycosporine-like Amino Acid Porphyra-334. *J. Phys. Chem. A* **2022**, *126*, 7460−7467.

(24) Whittock, A. L.; Abiola, T. T.; Stavros, V. G. A Perspective on Femtosecond Pump-Probe Spectroscopy in the Development of Future Sunscreens. *J. Phys. Chem. A* **2022**, *126*, 2299−2308.

(25) Whittock, A. L.; Auckloo, N.; Cowden, A. M.; Turner, M. A. P.; Woolley, J. M.; Wills, M.; Corre, C.; Stavros, V. G. Exploring the Blueprint of Photoprotection in Mycosporine-like Amino Acids. *J. Phys. Chem. Lett.* **2021**, *12*, 3641−3646.

(26) Kageyama, H.; Waditee-Sirisattha, R. Chapter 5—Mycosporine-Like Amino Acids as Multifunctional Secondary Metabolites in Cyanobacteria: From Biochemical to Application Aspects. In *Studies in Natural Products Chemistry*; Atta ur, R., Ed.; Elsevier, 2018; Vol. 59, pp 153−194.

(27) de Vries, M. S.; Hobza, P. Gas-phase spectroscopy of biomolecular building blocks. *Annu. Rev. Phys. Chem.* **2007**, *58*, 585−612.
(28) Sobolewski, A. L.; Domcke, W. Molecular mechanisms of the photostability of life. *Phys. Chem. Chem. Phys.* **2010**, *12*, 4897−4898.
(29) Watts, K. S.; Dalal, P.; Tebben, A. J.; Cheney, D. L.; Shelley, J. C. Macrocycle Conformational Sampling with MacroModel. *J. Chem. Inf. Model.* **2014**, *54*, 2680−2696.
(30) Halgren, T. A. Merck molecular force field. I. Basis, form, scope, parameterization, and performance of MMFF94. *J. Comput. Chem.* **1996**, *17*, 490−519.
(31) Dunning, T., Jr. Gaussian basis sets for use in correlated molecular calculations. I. The atoms boron through neon and hydrogen. *J. Chem. Phys.* **1989**, *90*, 1007−1023.
(32) Chai, J.-D.; Head-Gordon, M. Long-range corrected hybrid density functionals with damped atom−atom dispersion corrections. *Phys. Chem. Chem. Phys.* **2008**, *10*, 6615−6620.
(33) Finley, J.; Malmqvist, P.-Å.; Roos, B. O.; Serrano-Andrés, L. The multi-state CASPT2 method. *Chem. Phys. Lett.* **1998**, *288*, 299−306.
(34) Ahlrichs, R.; Bär, M.; Häser, M.; Horn, H.; Kölmel, C. Electronic Structure Calculations on Workstation Computers: The Program System Turbomole. *Chem. Phys. Lett.* **1989**, *162*, 165−169.
(35) *TURBOMOLE V6.3, a Development of University of Karlsruhe and Forschungszentrum Karlsruhe GmbH, 1989-2007*; TURBOMOLE GmbH, since 2007. Available from http://www.turbomole.com.
(36) Frisch, M. J.; Trucks, G. W.; Schlegel, H. B.; Scuseria, G. E.; Robb, M. A.; Cheeseman, J. R.; Scalmani, G.; Barone, V.; Petersson, G. A.; Nakatsuji, H.; et al. *Gaussian 16*, Rev. C.01; Gaussian, Inc.: Wallingford, CT, 2016.
(37) Celani, P.; Werner, H.-J. Multireference perturbation theory for large restricted and selected active space reference wave functions. *J. Chem. Phys.* **2000**, *112*, 5546−5557.
(38) Werner, H. J.; Knowles, P. J. A second order multiconfiguration SCF procedure with optimum convergence. *J. Chem. Phys.* **1985**, *82*, 5053−5063.
(39) Fdez. Galván, I.; Vacher, M.; Alavi, A.; Angeli, C.; Aquilante, F.; Autschbach, J.; Bao, J. J.; Bokarev, S. I.; Bogdanov, N. A.; Carlson, R. K.; et al. OpenMolcas: From Source Code to Insight. *J. Chem. Theory Comput.* **2019**, *15*, 5925−5964.
(40) Aquilante, F.; Autschbach, J.; Baiardi, A.; Battaglia, S.; Borin, V. A.; Chibotaru, L. F.; Conti, I.; De Vico, L.; Delcey, M.; Fdez, I.; et al. Modern quantum chemistry with Open-Molcas. *J. Chem. Phys.* **2020**, *152*, 214117.
(41) Abedini, F.; Omidyan, R.; Salehi, M. Theoretical insights on nonradiative deactivation mechanisms of protonated xanthine. *J. Photochem. Photobiol., A* **2019**, *385*, 112067.
(42) Shahrokh, L.; Omidyan, R.; Azimi, G. Excited state deactivation mechanisms of protonated adenine: a theoretical study. *Phys. Chem. Chem. Phys.* **2022**, *24*, 14898−14908.
(43) Omidyan, R.; Abedini, F.; Shahrokh, L.; Azimi, G. Excited State Deactivation Mechanism in Protonated Uracil: New Insights from Theoretical Studies. *J. Phys. Chem. A* **2020**, *124*, 5089−5097.
(44) Shahrokh, L.; Omidyan, R.; Azimi, G. Theoretical insights on the excited-state-deactivation mechanisms of protonated thymine and cytosine. *Phys. Chem. Chem. Phys.* **2021**, *23*, 8916−8925.
(45) Tuna, D.; Sobolewski, A. L.; Domcke, W. Mechanisms of Ultrafast Excited-State Deactivation in Adenosine. *J. Phys. Chem. A* **2014**, *118*, 122−127.
(46) Plasser, F.; Crespo-Otero, R.; Pederzoli, M.; Pittner, J.; Lischka, H.; Barbatti, M. Surface hopping dynamics with correlated single-reference methods: 9H-adenine as a case study. *J. Chem. Theory Comput.* **2014**, *10*, 1395−1405.
(47) Malmqvist, P.-Å.; Roos, B. O. The CASSCF state interaction method. *Chem. Phys. Lett.* **1989**, *155*, 189−194.
(48) Barbatti, M.; Ruckenbauer, M.; Plasser, F.; Pittner, J.; Granucci, G.; Persico, M.; Lischka, H. Newton-X: a surface-hopping program for nonadiabatic molecular dynamics. *Wiley Interdiscip. Rev.: Comput. Mol. Sci.* **2014**, *4*, 26−33.
(49) Abiola, T. T.; Rodrigues, N. d. N.; Ho, C.; Coxon, D. J. L.; Horbury, M. D.; Toldo, J. M.; do Casal, M. T.; Rioux, B.; Peyrot, C.; Mention, M. M.; Balaguer, P.; Barbatti, M.; Allais, F.; Stavros, V. G. New Generation UV-A Filters: Understanding Their Photodynamics on a Human Skin Mimic. *J. Phys. Chem. Lett.* **2021**, *12*, 337−344.
(50) Suh, S. S.; Hwang, J.; Park, M.; Seo, H. H.; Kim, H. S.; Lee, J. H.; Moh, S. H.; Lee, T. K. Anti-inflammation activities of mycosporine-like amino acids (MAAs) in response to UV radiation suggest potential anti-skin aging activity. *Mar. Drugs* **2014**, *12*, 5174−5187.
(51) Fazzi, D.; Barbatti, M.; Thiel, W. Unveiling the Role of Hot Charge-Transfer States in Molecular Aggregates via Nonadiabatic Dynamics. *J. Am. Chem. Soc.* **2016**, *138*, 4502−4511.
(52) Plasser, F.; Barbatti, M.; Aquino, A. J. A.; Lischka, H. Excited-State Diproton Transfer in [2,2′-Bipyridyl]-3,3′-diol: the Mechanism Is Sequential, Not Concerted. *J. Phys. Chem. A* **2009**, *113*, 8490−8499.
(53) Mennucci, B.; Cancès, E.; Tomasi, J. Evaluation of Solvent Effects in Isotropic and Anisotropic Dielectrics and in Ionic Solutions with a Unified Integral Equation Method: Theoretical Bases, Computational Implementation, and Numerical Applications. *J. Phys. Chem. B* **1997**, *101*, 10506−10517.
(54) Kinoshita, S.-n.; Miyazaki, Y.; Sumida, M.; Onitsuka, Y.; Kohguchi, H.; Inokuchi, Y.; Akai, N.; Shiraogawa, T.; Ehara, M.; Yamazaki, K.; Harabuchi, Y.; Maeda, S.; Taketsugu, T.; Ebata, T. Different photoisomerization routes found in the structural isomers of hydroxy methylcinnamate. *Phys. Chem. Chem. Phys.* **2018**, *20*, 17583−17598.
(55) Kinoshita, S.-n.; Inokuchi, Y.; Onitsuka, Y.; Kohguchi, H.; Akai, N.; Shiraogawa, T.; Ehara, M.; Yamazaki, K.; Harabuchi, Y.; Maeda, S.; Ebata, T. The direct observation of the doorway 1nπ^* state of methylcinnamate and hydrogen-bonding effects on the photochemistry of cinnamate-based sunscreens. *Phys. Chem. Chem. Phys.* **2019**, *21*, 19755−19763.
(56) Toldo, J. M.; do Casal, M. T.; Barbatti, M. Mechanistic Aspects of the Photophysics of UVA Filters Based on Meldrum Derivatives. *J. Phys. Chem. A* **2021**, *125*, 5499−5508.
(57) Abiola, T. T.; Rioux, B.; Toldo, J. M.; Alarcan, J.; Woolley, J. M.; Turner, M. A. P.; Coxon, D. J. L.; Telles do Casal, M.; Peyrot, C.; Mention, M. M.; Buma, W. J.; Ashfold, M. N. R.; Braeuning, A.; Barbatti, M.; Stavros, V. G.; Allais, F. Towards developing novel and sustainable molecular light-to-heat converters. *Chem. Sci.* **2021**, *12*, 15239−15252.
(58) Barbatti, M.; Sen, K. Effects of different initial condition samplings on photodynamics and spectrum of pyrrole. *Int. J. Quantum Chem.* **2016**, *116*, 762−771.
(59) Cardozo, T. M.; Galliez, A. P.; Borges, I.; Plasser, F.; Aquino, A. J. A.; Barbatti, M.; Lischka, H. Dynamics of benzene excimer formation from the parallel-displaced dimer. *Phys. Chem. Chem. Phys.* **2019**, *21*, 13916−13924.
(60) Lischka, H.; Barbatti, M.; Siddique, F.; Das, A.; Aquino, A. J. A. The effect of hydrogen bonding on the nonadiabatic dynamics of a thymine-water cluster. *Chem. Phys.* **2018**, *515*, 472−479.
(61) Crespo-Otero, R.; Barbatti, M. Spectrum simulation and decomposition with nuclear ensemble: formal derivation and application to benzene, furan and 2-phenylfuran. In *Marco Antonio Chaer Nascimento: A Festschrift from Theoretical Chemistry Accounts*; Ornellas, F. R., João Ramos, M., Eds.; Springer Berlin Heidelberg: Berlin, Heidelberg, 2014; pp 89−102.
(62) Swope, W. C.; Andersen, H. C.; Berens, P. H.; Wilson, K. R. A computer simulation method for the calculation of equilibrium constants for the formation of physical clusters of molecules: Application to small water clusters. *J. Chem. Phys.* **1982**, *76*, 637−649.
(63) Granucci, G.; Persico, M. Critical appraisal of the fewest switches algorithm for surface hopping. *J. Chem. Phys.* **2007**, *126*, 134114.
(64) Tully, J. C. Molecular dynamics with electronic transitions. *J. Chem. Phys.* **1990**, *93*, 1061−1071.

https://doi.org/10.1021/acs.jpca.3c02360
J. Phys. Chem. A 2023, 127, 4880−4887